electronic materials

MDPI

Article

Magnetization of Magnetically Inhomogeneous $Sr_2FeMoO_{6-\delta}$ Nanoparticles

Gunnar Suchaneck [1,*], Nikolai Kalanda [2], Marta Yarmolich [2], Evgenii Artiukh [1,2], Gerald Gerlach [1] and Nikolai A. Sobolev [3,4]

1 Solid-State Electronics Laboratory, TU Dresden, 01062 Dresden, Germany; sirfranzferdinand@yandex.ru (E.A.); Gerald.Gerlach@tu-dresden.de (G.G.)
2 Cryogenic Research Division, Scientific-Practical Materials Research Centre of NAS of Belarus (SSPA), 220072 Minsk, Belarus; kalanda362@gmail.com (N.K.); martochka_ymv@mail.ru (M.Y.)
3 i3N and Departamento de Física, Universidade de Aveiro, 3810-193 Aveiro, Portugal; sobolev@ua.pt
4 Laboratory of Functional Low-Dimensional Structures, National University of Science and Technology "MISiS", 119049 Moscow, Russia
* Correspondence: gunnar.suchaneck@tu-dresden.de

Abstract: In this work, we describe the magnetization of nanosized SFMO particles with a narrow size distribution around ca. 70 nm fabricated by the citrate-gel technique. The single-phase composition and superstructure ordering degree were proved by X-ray diffraction, the superparamagnetic behavior by magnetization measurements using zero-field cooled and field-cooled protocols, as well as by electron magnetic resonance. Different contributions to the magnetic anisotropy constant and the temperature dependence of the magnetocrystalline anisotropy are discussed.

Keywords: strontium ferromolybdate; citrate-gel process; nanoparticles; magnetization

Citation: Suchaneck, G.; Kalanda, N.; Yarmolich, M.; Artiukh, E.; Gerlach, G.; Sobolev, N.A. Magnetization of Magnetically Inhomogeneous $Sr_2FeMoO_{6-\delta}$ Nanoparticles. *Electron. Mater.* **2022**, *3*, 82–92. https://doi.org/10.3390/electronicmat3010008

Academic Editor: Andrzej Molak

Received: 13 December 2021
Accepted: 26 January 2022
Published: 8 February 2022

1. Introduction

Strontium ferromolybdate ($Sr_2FeMoO_{6-\delta}$, SFMO) is a widely studied ferrimagnetic double perovskite. SFMO is a promising candidate for magnetic electrode materials for room-temperature spintronic applications, because they present a half-metallic character (with theoretically 100% polarization), a high Curie temperature (T_C) of about 415 K (ferromagnets should be operated in their ordered magnetic state below T_C), and a low-field magnetoresistance [1]. The same is valid for its derivatives such as (SrBa)$FeMoO_{6-\delta}$ or (SrLa)$FeMoO_{6-\delta}$. However, wide application of SFMO is still missing, because of the low reproducibility of its magnetic properties originating in ceramic processing issues and its ageing upon contact with air and moisture. SFMO is a material which properties are very sensitive to disordering at the B-site, i.e., Fe_{Mo} and Mo_{Fe} antisite defect formation, nonstoichiometry of the magnetic Fe ions, and, with a lesser extent, to oxygen- and Sr-deficit [2].

Recently, an inhomogeneous magnetic state was obtained in SFMO nanoparticles fabricated by solid-state reactions from partially reduced $SrFeO_{3-x}$ and $SrMoO_4$ precursors by studying the temperature dependences of the magnetization measured in the field-cooling (FC) and zero-field-cooling (ZFC) modes and small-angle neutron scattering [3]. This state was attributed to the frustration of the exchange bonds and simultaneous occurrence of various magnetic states: antiferromagnetic, ferrimagnetic, and superparamagnetic when the spin inversion does not change the energy of the system in a wide range of temperatures. In another report [4], the Mössbauer spectrum of SFMO fine particles of about 30 nm size, consisting of small traces of $SrMoO_4$, revealed a paramagnetic doublet above a blocking temperature T_B = 45 K, while the spectrum of a similar sample with a size of 197 nm taken at 77 K included superparamagnetic, ferromagnetic and surface contributions. Diverse magnetic behavior - superparamagnetic, ferromagnetic and paramagnetic–was detected in

single-phase $Mg_xZn_{1-x}Fe_2O_4$ nanoparticles by Mössbauer spectroscopy and curve fitting of the magnetic-field dependence of the magnetization [5]. This was attributed to the distribution of particle sizes in the samples.

In this work, we determine the magnetization behavior of nanosized magnetically inhomogeneous SFMO particles by means of ZFC-FC magnetization and electron magnetic resonance measurements. Furthermore, we discuss different contributions to magnetic anisotropy and evaluate the temperature dependence of the uniaxial magnetocrystalline anisotropy constant.

2. Materials and Methods

The citrate-gel technique was used for the synthesis of SFMO nanoparticles using ultra-high purity $Sr(NO_3)_2$, $Fe(NO_3)_3{\cdot}9H_2O$, $(NH_4)_6Mo_7O_{24}$ and citric acid monohydrate $C_6H_8O_7H_2O$ as initial reagents. The solid foam resulting from the synthesis was crushed and annealed at T = 770 K and $p_{O2} = 2.1{\times}10^4$ Pa for 10 h. After that, the powders were annealed in a 5% H_2/Ar gas mixture flow at 1170 K for 5 h, followed by quenching at room temperature. Synthesis details are described in Ref. [6] (cf. Supplemental Materials, Figure S1). Since the SFMO powders were agglomerated, ultrasonic dispersion as used to obtain highly dispersed particles with an average size smaller than 100 nm. Ethyl alcohol was chosen as a liquid medium since there is neither chemical interaction with SFMO nor SFMO decomposition.

To optimize the process of SFMO dispersion, the effects of time and radiation power of the ultrasonic homogenizer on the dispersion of the particles were studied in a suspension of 0.1 g of powder per 25 mL of C_2H_5OH. The power of ultrasonic exposure was varied from 1% to 100% of the nominal power (P_n) with a step of 25% at a frequency of 22 kHz and an exposure time ranging from 15 to 60 min with a step of 15 min. To prevent the process of coagulation of SFMO grains, different surfactants were used. The surfactant was selected to achieve a high Z-potential. Cationic hexadecyltrimethylammonium bromide, anionic sodium tripolyphosphate, nonionic polyoxyethylene (20) sorbitan monolaurate Tween20^{TM}, and nonionic polycarboxylate/sodium salt Dolapix PC 67 were tested. The most suitable was the nonionic Tween20^{TM} surfactant providing the main results described in this work. In this case, the Zeta potential of SFMO nanopowder has negative values. The highest values of the Zeta potential (Z = −63.2 mV) in 25 mL (C_2H_5OH) + 0.01 g SFMO + x g Tween 20^{TM} subjected to dispersion for 45 min was achieved at x = 0.05 g Tween20^{TM}.

X-ray diffraction (XRD) patterns of samples with a weight of ca. 60 mg were recorded at room temperature at a rate of 60°/h in the range of angles Θ = 10–90° using a DRON-3 diffractometer (Bourevestnik, Saint Petersburg, Russia) in CuK_α radiation and analyzed by means of the ICSD-PDF2 database (Release 2000) and PowderCell software. The microstructure, morphology, and elemental composition of grains of annealed SFMO powders were investigated by field-emission scanning electron microscope JEOL JSM-7000F (JEOL Ltd., Tokyo, Japan). The grain sizes were estimated by an NT-206 atomic force microscope (Microtestmachines, Gomel, Belarus). The particle size distribution was obtained by dynamic light scattering (DLS) analysis using a Zetasizer Nanoparticles analyzer (Malvern Nano ZS90, Malvern, UK).

Magnetization measurements of the samples were performed at magnetic fields up to 4 T in a temperature range from 4.2 K to 320 K using a Liquid Helium-Free High-Field Measurement System vibrating sample magnetometer (Cryogenic Ltd., London, UK). ZFC-FC curves were acquired in a magnetic field of 0.01 T.

The electron magnetic resonance (EMR) measurements of samples with a weight of ca. 20 mg were performed in the X-band (9.45 GHz) at a field modulation frequency of 100 kHz using an EleXsys E-500 electron paramagnetic resonance spectrometer (Bruker, Billerica, MA, USA) equipped with a nitrogen-flow cryostat. The first field derivative of the microwave absorption, $dP_{mw}/dB \propto d\chi''/dB$, with P_{mw} the microwave power and χ'' the imaginary part of the magnetic AC susceptibility, was registered. The magnetic field was swept from high to low values.

3. Results

Single-phase SFMO powders were obtained with crystal lattice parameters $a = b = 0.55629$ nm, $c = 0.78936$ nm and with a B-site superstructural ordering degree of 88% (cf. Supplemental Materials, Figures S2 and S3). After ultrasonic treatment, the sizes of agglomerates in a suspension of 25 mL (C_2H_5OH) + 0.01 g (SFMO) + 0.05 g (Tween 20), subjected to sonication for 60 min, smoothly decrease from 230 nm to about 70 nm (Figure 1). At an ultrasonic power of $P = 25\%\ P_n$, a release of dissolved gases begins in the rarefaction regions being at low pressure, which is accompanied by the formation of a durable bubble. The latter is stabilized by a monolayer of SFMO particles and oscillates linearly with the frequency of the ultrasonic wave relatively to its equilibrium position. Here, dispersion is less effective. A further increase of the power up to $P = 75\%\ P_n$ leads to a violation of linearity of oscillations of the bubble walls. The stage of stable cavitation begins. The bubble itself becomes a source of ultrasonic higher-harmonic vibrations. Waves, microcurrents and electric discharges appear on its surface [7,8]. This increases the dispersion of SFMO particles. Thus, at sonication times up to 45 min, particles are effectively dispersed in the entire suspension volume, and processes of coagulation and sedimentation of particles are prevented. The ultrasonic wave passing through the liquid creates zones of compression and depression, which alternate in each half-period of the wave. For this reason, the particles of the medium vibrate with small amplitudes (in the sub-μm range) and huge accelerations [7,8]. A further increase of p beyond 75% P_n leads to unstable cavitation and the formation of a cavitation cloud on the surface of the alcohol solution, which hinders the transmission of ultrasonic vibrations into the volume [7,8]. This state of the alcohol suspension is characterized by the formation of rapidly growing vapor-gas bubbles, which instantly contract in volume during the compression phase and collapse. Because of this, the average particle size increases again up to 450 nm as a result of ultrasonic treatment with $P = P_n$ for times up to 60 min. This indicates intensive coagulation prevailing over the dispersion process, which can be explained by the formation of a cavitation cloud (a large number of air bubbles) on the surface of the working tool hindering the transmission of ultrasonic vibrations into the volume and, thus, reducing the grinding efficiency. Saturation of particle size was reached after 80 min ultrasonic treatment. Figure 2 illustrates the increase of the volume fraction of fine SFMO particles with sonication time.

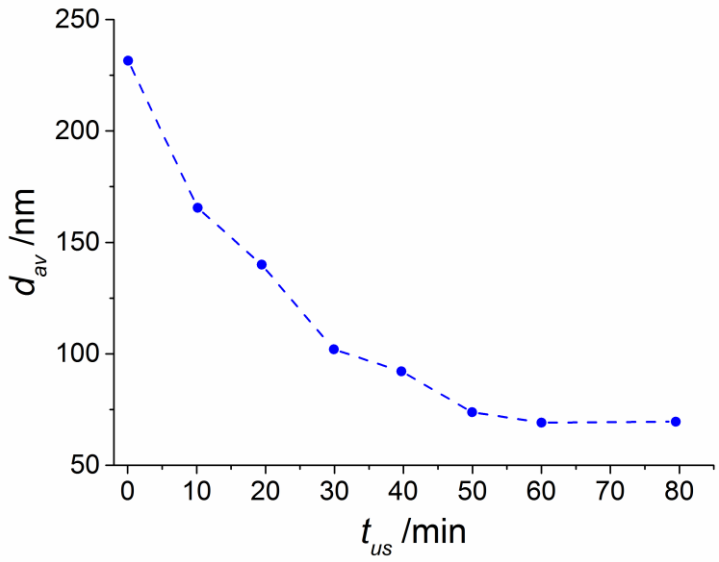

Figure 1. Dependence of the SFMO agglomerate size on sonication time.

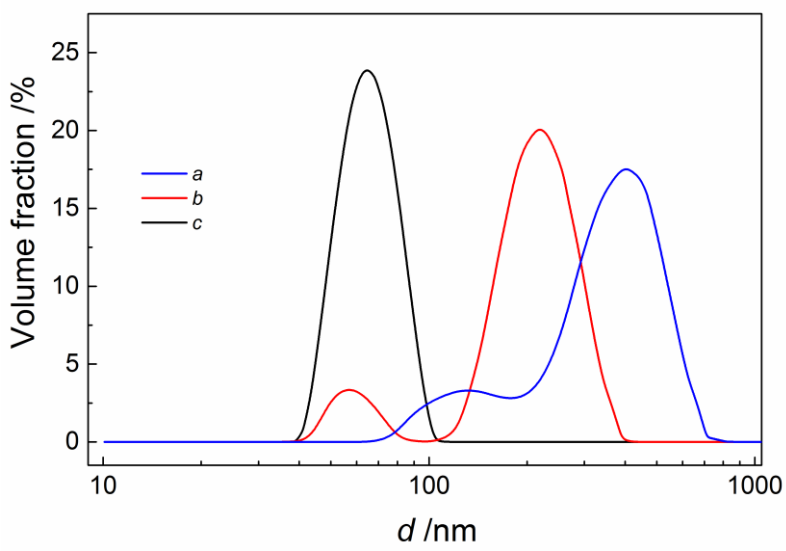

Figure 2. Volume fraction of particles with size d for sonication times t_{us} of (*a*) 10 min, (*b*) 15 min, and (*c*) 60 min.

The nanoparticle size distribution was analyzed by means of DLS. It is most widely represented by the lognormal distribution:

$$f(d) = \frac{1}{\sqrt{2\pi}d\sigma} \exp\left\{ -\frac{[\ln(d) - \ln(d_{av})]^2}{2\sigma^2} \right\} \quad (1)$$

where d_{av} and σ are the average diameter and dispersion of the particle size distribution, respectively [9]. The calculated average particle diameter for the powder subjected to sonication for 60 min amounts to d_{av} = 67.8 nm and the dispersion to σ = 0.214 nm (Figure 3).

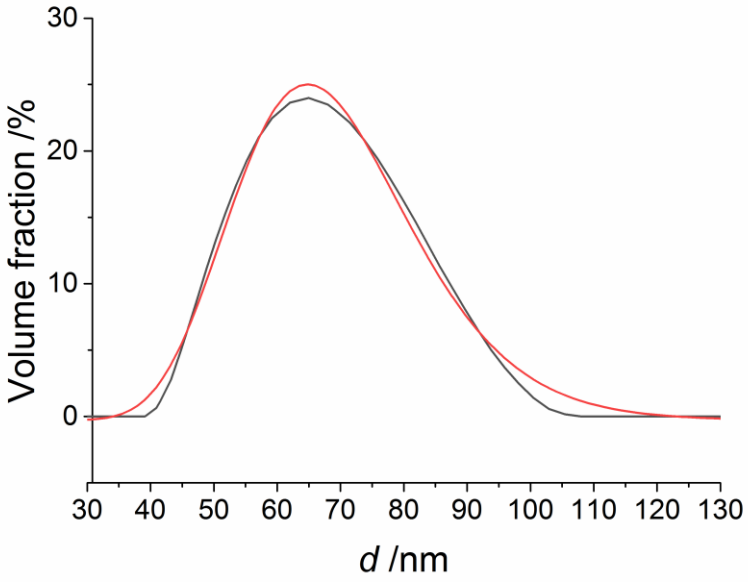

Figure 3. Size distribution of the volume fraction of an ensemble of SFMO nanoparticles after ultrasonic dispersion for 60 min determined by DLS analysis (black line) and its approximation by the log-normalized function $f(d)$ (red line).

Figure 4 shows a scanning electron microscopy image of the as-fabricated, agglomerated SFMO nanoparticles (Figure 4a) and an atomic force microscopy (AFM) scan of the nanoparticles on a substrate (Figure 4b). The figures demonstrate a narrow size distribution of particles with a size in the order of 70 nm and the de-agglomeration after ultrasonic treatment. The height of the AFM features corresponds approximately to the average particle size obtained by DLS. Note that features with a size of about 10 nm could not be resolved by AFM.

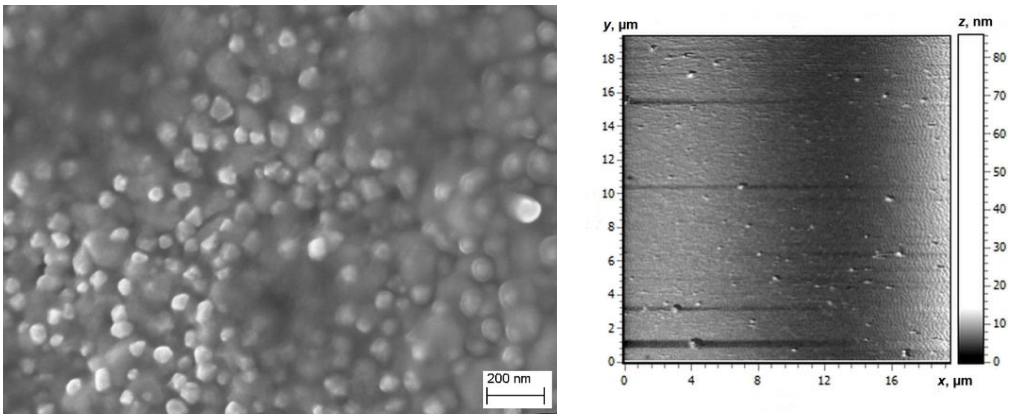

(**a**) (**b**)

Figure 4. Scanning electron microscopy image as the as-fabricated, agglomerated SFMO nanoparticles (**a**) and an atomic force microscopy scan of the nanoparticles on a substrate (**b**).

Measurements of the temperature dependence of the magnetization following the ZFC-FC protocol revealed the presence of at least superparamagnetic and metastable blocked behavior (Figure 5) (cf. [4]). The maximum of the ZFC curve is located at a maximum temperature T_{max} of ca. 20 K. The low blocking temperature, as well as a large increment of magnetization with decreasing temperature in the FC data, reveal that the magnetic interaction between the nanoparticles is quite weak. With regard to the lognormal size distribution, the position of T_{max} is not the same as the average blocking temperature T_B. The latter is shifted down to smaller values by a correction factor of 1.5 [10] giving rise to $T_B \approx 13$ K. The corresponding $K_1 V$ value amounts to 5.25×10^{-21} J. Note that the difference between the maximum position of the ZFC curve at 20 K and the bifurcation point between the ZFC and FC curves at ca. 170 K is another measure of the dispersion of grain sizes [11]: the biggest particles are deblocked at the latter temperature. Also, we have to take into account that the value of T_B depends on the applied magnetic field. Following a model proposed in [12], we found that in our case T_B is underestimated by about 7%.

In Figure 6a, EMR spectra of a similar SFMO sample with a B-site superstructure ordering degree of 81% are plotted for measurement temperatures ranging from 120 K to 480 K. Figure 6b shows the corresponding resonant magnetic field B_r, defined as the field for which the derivative dP_{mw}/dB goes through zero, and the linewidth ΔB_{pp} defined as the field interval between the positive and negative peaks of the resonance curve. The signal reduces rapidly at temperatures above 400 K, however, the line is still observable at 440 K and completely disappears at 460 K. Thus, the Curie temperature T_C is slightly above 400 K (the FMR is usually observed even at the paramagnetic side of T_C [13]). The resonance field B_r is always below that of the paramagnetic resonance value corresponding to $g = 2$ and approaches the latter with increasing temperature. As the temperature decreases below T_C, the spectra are broadened and shift towards lower magnetic fields. The latter effect is typical of predominantly cubic magnetic anisotropy.

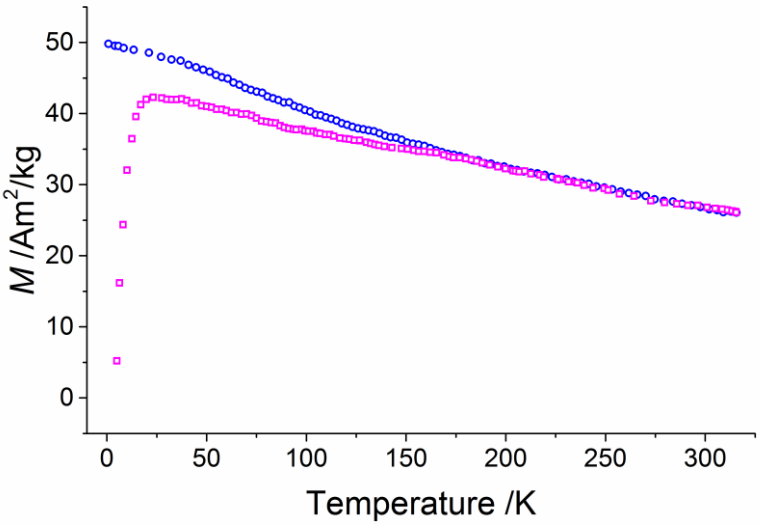

Figure 5. Magnetization of the fabricated SFMO nanoparticles in the FC mode (blue dots) and in the ZFC mode (magenta squares).

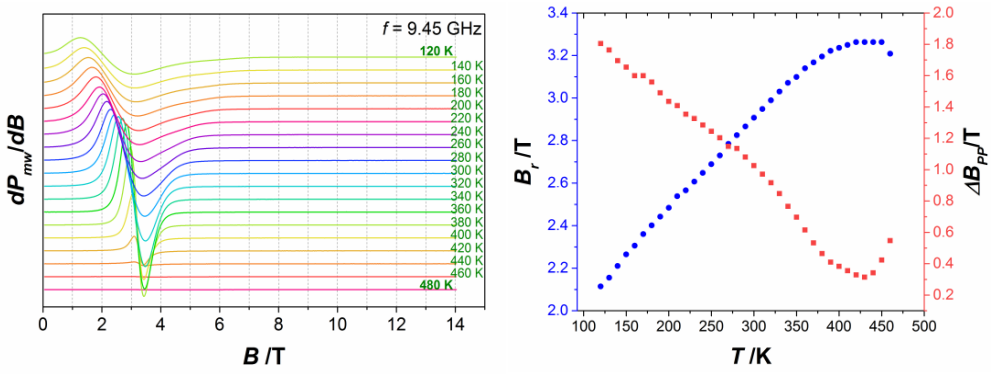

(**a**) (**b**)

Figure 6. Temperature dependence of the EMR spectra (**a**), resonance field B_r and peak-to-peak linewidth ΔB_{pp} (**b**).

Since in magnetic resonance measurements in the X-band the characteristic measurement time τ_m amounts to 10^{-10} s, the characteristic blocking temperature is roughly given by $kT_B \approx K_1 V$ [14]. Considering ZFC magnetization measurements, this yields $T_B^{EMR} \approx 330$ K. Unfortunately, passing through 330 K produces no clear effect on the curves in Figure 6b. In [14], the T_B value has been obtained by plotting the total intensity (second integral) of the experimental EMR absorption band versus temperature. However, this method is rather imprecise when a part of the resonance band is not recorded as is the case at low temperatures.

The linewidth is determined by the spread of the resonance fields of the individual nanoparticles caused by the random distribution of their easy magnetization axes and by the precession damping of the magnetic moments. The spontaneous magnetization can contribute to the linewidth of individual grains via its site-to-site distributions concerning both the Zeeman and the magnetostatic energy terms [14]. With lowering temperature, the thermal fluctuation energy becomes smaller than the anisotropy energy. Here, the random thermal fluctuation field $B_f \sim kT/\mu_{eff}$ (with μ_{eff} being the effective magnetic moment of the superparamagnetic particle) diminishes [15], thus broadening the linewidth. Another reason for the temperature-dependent broadening is the variation of the anisotropy energy with temperature.

At very low temperatures, the spin-wave spectrum of nanoparticles is quantized with a dominating uniform mode $n = 0$ [16]. This results in a linear temperature dependence of magnetization:

$$M(T) \approx M(0)\left(1 - \frac{kT}{2K_1V}\right) \tag{2}$$

Fitting the asymptote of the low-temperature part of $M(T)$ to Equation (2), we obtain $K_1V \approx 5.0 \times 10^{-21}$ J in good agreement with the value derived above from the blocking temperature. Divided by the superparamagnetic particle volume this yields $K_1' \approx 5.0 \times 10^3$ J/m^3.

In our case, we have to take into account that the size of our particles is above the superparamagnetic limit of about 10.5 nm, Equation (6). Here, a correction factor $(1 - H/H_c)^2$ appears for the K_1V value [17]. For $K_1 \approx 1.7 \times 10^5$ J/m^3 (cf. Section 4), we find $\mu_0 H_c \approx 12$ mT (the measuring field was $\mu_0 H = 10$ mT) in accordance with the experimental value of $\mu_0 H_c \approx 12$–14 mT at 4.2 K of similar samples, but pressed into pellets and long-term annealed at 1420 K in a flux of a gas mixture of 5% H_2/Ar [18].

4. Discussion

The remanent magnetization of uniaxial, single-domain nanoparticles which are fully magnetized along the easy axis vanishes after removing the magnetic field as:

$$M = M_s \exp\left(-\frac{t}{\tau}\right) \tag{3}$$

where M_s is the saturation magnetization, t the time after removal of the field. The value τ denotes the Néel-Brown relaxation time for an energy barrier $\Delta E = K_1V$ [19,20]:

$$\tau = \tau_0 \exp\left(\frac{K_1V}{kT}\right) \tag{4}$$

with τ_0 a time constant in the order of 10^{-9} s [21], K_1 the uniaxial anisotropy constant, V the particle volume, k the Boltzmann constant and T the temperature. Note that K_1 is also temperature dependent [22]. Superparamagnetic behavior is obtained using an instrument with a characteristic measuring time $\tau_m \geq \tau$. For $\tau_m < \tau$, the magnetic moments remain in a fixed direction during the measurement. This leads to a remanent magnetization and appearance of a coercive field, thus, a metastable ferromagnetic (ferrimagnetic) state is detected. The condition $\tau = \tau_m$ defines the so-called blocking temperature [23]:

$$T_B = \frac{K_1V}{k \cdot \ln(\tau_m/\tau_0)} \tag{5}$$

Here, τ_m amounts to ca. 100 s in static magnetometry [24], and to $\tau_m \approx 10^{-8}$ s in Mössbauer spectrometry [23]. Simultaneous ferromagnetic and SPM behavior is obtained when τ is of the order of τ_m. Thus, particles at a temperature $T > T_B$ reveal a dominating SPM behavior, while particles at $T < T_B$ show a predominant ferromagnetic behavior. In the latter case thermal excitations are not sufficient to overcome the barrier K_1V. The easiest way to implement such conditions is to use a mixture of particles of different sizes slightly below and slightly above a critical size, which for spherical particles amounts to:

$$d_{cr}^{spm} = \left(\frac{q \cdot kT}{K_1(T)}\right)^{1/3} \tag{6}$$

where the parameter $q = \pi/6 \cdot \ln(\tau_m/\tau_0)$ amounts in magnetometry to ca. 48 and in Mössbauer spectrometry to ca. 4.4.

In the simplest form of uniaxial anisotropy, the total free energy U of a particle is given by [24]:

$$U = K_1V \sin^2\varphi - uH\cos\varphi \tag{7}$$

where φ is the angle between μ and the symmetry axis of the particle. Experimental values of K_1 for SFMO are scarce. EMR measurements on SFMO thin films grown by pulsed laser deposition onto (100) $SrTiO_3$ substrates with a thickness of 400 nm revealed for M_s = 3.8 μ_B an in-plane uniaxial magnetocrystalline anisotropy constant of ca. 3×10^4 J/m^3 at room temperature [25]. On the other hand, the estimated zero-temperature value of K_1 is much higher and amounts to 1.7×10^5 J/m^3 [26]. This is the low-temperature value used in the present work.

The shape-anisotropy constant calculated employing demagnetization factors γ in the c and a directions [27] is given by:

$$K_{sh} = \frac{1}{2}(\gamma_c - \gamma_a) u_0 M_s^2 \tag{8}$$

Here, μ_0 is the vacuum permeability. Optical inspection of the particle shape revealed that the latter is well approximated by oblate spheroids with a c/a ratio in the range from 0.85 to 1.0. With M_s = 282 kA/m (50 Am^2/kg), this results in a negligible value of $K_{sh} \leq 3.3 \times 10^3$ J/m^3.

Inhomogeneous surface conditions during synthesis yield an effective anisotropy constant of [28,29]:

$$K_{eff} = K_V + \frac{S}{V} K_S(d) \tag{9}$$

where K_V is the anisotropy constant per unit volume, K_S the surface anisotropy constant per unit of surface area S, and d the particle size. For a sphere or cube, the total surface-area-to-volume ratio amounts to $6/d$. Surface anisotropy arises due to symmetry breaking and reduction in the nearest-neighbor coordination at the surface. It can significantly enhance the total magnetic anisotropy of nanoparticles. For instance, K_{eff} of γ-Fe_2O_3 nanoparticles with a mean size of about 8.6 nm dispersed in a polymer exceeds K_V by about two orders of magnitude [30]. However, in our case, the surface conditions after a long-time ultrasonic treatment are mostly balanced. On the other hand, strains relax in homogeneous, twin-free nanoparticles, that have no shell or grain boundary. Therefore, only the particle size needs to be considered as the origin of the simultaneous observation of ferromagnetic and superparamagnetic behavior. As a result, we have only to account for the magnetocrystalline anisotropy constant.

Replotting B_r in Figure 6b using a reduced temperature $\vartheta = (1 - T/T_C)$, we obtain a slope of $dB_r/d\vartheta = -1.825$ T (cf. Supplemental Materials, Figure S4). The shift of B_r is determined by the temperature dependence of the magnetic anisotropy field:

$$H_a(T) = \frac{2\alpha K_1(T)}{\mu_0 M(T)} \tag{10}$$

where α is an averaged factor, which depends only on the angles between the applied field and the magnetic axes of the particles. A satisfactory approximation of the temperature dependence of the magnetization derived from Monte-Carlo and Landau–Lifshitz–Gilbert simulations is $M(T) = M(0) \cdot \vartheta^{1/3}$ [31]. With regard to the linear temperature dependence of B_r, we conclude

$$K_1(T) = K_1(0) \cdot (1 - T/T_C)^{4/3} \tag{11}$$

Taking into account $dB_r/d\vartheta = -1.825$ T, for M_s = 3.8 μ_B/f.u. we arrive at $2\alpha K_1(0) = 5.2 \times 10^5$ J/m^3, which is of the order of the values considered above. For $K_1(0\ \mathrm{K}) = 1.7 \times 10^5$ J/m^3 [26], Equation (11) yields a room-temperature value of $K_1(300\ \mathrm{K}) = 2.35 \times 10^4$ J/m^3 comparable to the in-plane uniaxial anisotropy constant of SFMO thin films amounting to ~3×10^4 J/m^3 at room temperature [25].

A lower limit of the critical diameter of a single-domain particle amounts to [32]:

$$d_{cr}^{sd} \geq \frac{36\sqrt{A(T) \cdot K_1(T)}}{u_0 M_s^2} \tag{12}$$

where $A(T)$ is the (temperature-dependent) exchange constant. An estimation of the A value using the spin-wave stiffness $D(T)$ [33], yields a low-temperature value $A(0) = 1.85 \times 10^{-12}$ J/m assuming $M_s(0) = 3.8\ \mu_B$/f.u. [26].

$$A(T) = \frac{D(T)M_s(T)}{2g\mu_B} \tag{13}$$

The temperature dependencies of $D(T)$ and $M_s(T)$ then determine $A(T)$. On the other hand, the reduced magnetization $m(T) = M(T)/M(0)$ of SFMO measured in the FC mode decreases from liquid helium temperatures to 120 K just by 12% (cf. Figure 5). Consequently, the temperature dependence of A can be neglected when calculating the size of superparamagnetic particles in the low-temperature range. The A value at room temperature was recently estimated to be $A(300\ \text{K}) = 9.2 \times 10^{-13}$ J/m [26].

As a result, the lower limit of the critical diameter ${d_{cr}}^{sd}$ of a single-domain particle according to Equation (12) was calculated to be 41 nm at low temperatures and ca. 68 nm near room temperature, that is, of the order of the nanoparticle size. The critical size of a spherical superparamagnetic particle ${d_{cr}}^{spm}$ (cf. Equation (6)) at room temperature amounts to 10.5 nm corresponding to a volume of 605 nm^3 and about 4900 spins. Obviously, particles with a size around ${d_{cr}}^{sd}$ determine the DLS while larger particles, though less numerous, dominate the magnetic response at high temperatures.

Alternatively, the magnetization behavior could be analyzed solely as a superposition of Langevin functions of various magnetic moments [29]. This would result in a broad distribution of μ in order to reproduce the steep slope of the $M(B)$ dependence (cf. Supplemental Materials, Figure S5).

5. Conclusions

Nanosized SFMO particles with a narrow size distribution around ca. 70 nm were fabricated by the citrate-gel technique. Single-phase composition and superstructure ordering degree were proved by X-ray diffraction. Superparamagnetic behavior was demonstrated by magnetization measurements using zero-field cooled and field-cooled protocols as well as by electron magnetic resonance. The linear slope of the shift of the resonance field B_r versus reduced temperature served as the basis for the derivation of an approximate 4/3 power dependency of the magnetocrystalline anisotropy constant on the reduced temperature $\vartheta = (1 - T/T_C)$. The origin of the simultaneous superparamagnetic and blocked behavior was attributed to a nanoparticle size distribution around a value in the order of the critical diameter of single-domain particles.

Supplementary Materials: The following are available online at https://www.mdpi.com/article/10.3390/electronicmat3010008/s1, Figure S1: Flow-chart of the fabrication of magnetically inhomogeneous $Sr_2FeMoO_{6-\delta}$ nanoparticles by the citrate-gel technique, Figure S2: X-ray diffraction pattern of the fabricated $Sr_2FeMoO_{6-\delta}$ nanoparticles, Figure S3: Comparison of the the superstructural (101) XRD peak of $Sr_2FeMoO_{6-\delta}$ with $p = 88\%$ (red squares) with the ideal structure with $p = 100\%$ (black solid line), Figure S4: Resonance field B_r versus reduced temperature $\vartheta = (1 - T/T_C)$. The linear part of the curve is marked by a red line, Figure S5: Field dependence of the magnetization of the SFMO nanoparticles.

Author Contributions: Conceptualization, G.S. and N.K.; methodology, G.S., M.Y. and E.A; software, E.A.; validation, G.S., N.K., G.G. and N.A.S.; formal analysis, E.A.; investigation, M.Y., E.A., N.K. and N.A.S.; resources, N.K.; data curation, N.K.; writing—original draft preparation, G.S., N.K. and N.A.S.; writing—review and editing, G.S. and N.A.S.; visualization, E.A.; supervision, project administration G.G., N.K. and N.A.S., funding acquisition, G.G. and N.A.S. All authors have read and agreed to the published version of the manuscript.

Funding: This research was funded by the European Union within the scope of the European project H2020-MSCA-RISE-2017-778308–SPINMULTIFILM.

Institutional Review Board Statement: Not applicable.

Informed Consent Statement: Not applicable.

Data Availability Statement: The original contributions presented in the study are included in the article/Supplemental Materials, further inquiries can be directed to the corresponding author.

Acknowledgments: The authors are grateful to A.A. Timopheev for fruitful discussions. They thank T. Zubar and B.M.S. Teixeira for support with AFM and EMR measurements, respectively.

Conflicts of Interest: The authors declare no conflict of interest.

References

1. Kobayashi, K.I.; Kimura, T.; Sawada, H.; Terakura, K.; Tokura, Y. Room-Temperature Magnetoresistance in an Oxide Material with an Ordered Double-Perovskite Structure. *Nature* **1998**, *395*, 677–680. [CrossRef]
2. Suchaneck, G.; Kalanda, N.; Artsiukh, E.; Gerlach, G. Challenges in $Sr_2FeMoO_{6-\delta}$ Thin Film Deposition. *Phys. Status Solidi* **2019**, *257*, 1900312. [CrossRef]
3. Kalanda, N.; Karpinsky, D.; Bobrikov, I.; Yarmolich, M.; Kuts, V.; Huang, L.; Hwang, C.; Kim, D.H. Interrelation among Superstructural Ordering, Oxygen Nonstoichiometry and Lattice Strain of Double Perovskite $Sr_2FeMoO_{6-\delta}$ Materials. *J. Mater. Sci.* **2021**, *56*, 11698–11710. [CrossRef]
4. Suominen, T.; Raittila, J.; Salminen, T.; Schlesier, K.; Lindén, J.; Paturi, P. Magnetic Properties of Fine SFMO Particles: Superparamagnetism. *J. Magn. Magn. Mater.* **2007**, *309*, 278–284. [CrossRef]
5. John, S.P.; Mathew, J. Determination of Ferromagnetic, Superparamagnetic and Paramagnetic Components of Magnetization and the Effect of Magnesium Substitution on Structural, Magnetic and Hyperfine Properties of Zinc Ferrite Nanoparticles. *J. Magn. Magn. Mater.* **2019**, *475*, 160–170. [CrossRef]
6. Suchaneck, G.; Kalanda, N.; Artiukh, E.; Yarmolich, M.; Sobolev, N.A. Tunneling Conduction Mechanisms in Strontium Ferromolybdate Ceramics with Strontium Molybdate Dielectric Intergrain Barriers. *J. Alloys Compd.* **2021**, *860*, 158526. [CrossRef]
7. Flynn, H.G. *Physical Acoustics*; Mason, W.P., Ed.; Academic Press: New York, NY, USA, 1964; Volume 1, Part B, pp. 57–172.
8. Gedanken, A. Using sonochemistry for the fabrication of nanomaterials. *Ultrason. Sonochem.* **2004**, *11*, 47–55. [CrossRef]
9. Granqvist, C.G.; Buhrman, R.A. Ultrafine Metal Particles. *J. Appl. Phys.* **1976**, *47*, 2200–2219. [CrossRef]
10. Coaquira, J.A.H.; Vaccari, C.B.; Tedesco, A.C.; Morais, P.C. Magnetic Investigation of $CoFe_2O_4$ Nanoparticles Supported in Biocompatible Polymeric Microsphere. *IEEE Trans. Magn.* **2009**, *45*, 4059–4062. [CrossRef]
11. Denardin, J.C.; Brandl, A.L.; Knobel, M.; Panissod, P.; Pakhomov, A.B.; Liu, H.; Zhang, X.X. Thermoremanence and zero-field-cooled/field-cooled magnetization study of $Co_x(SiO_2)_{1-x}$ granular films. *Phys. Rev. B—Condens. Matter Mater. Phys.* **2002**, *65*, 064422. [CrossRef]
12. El-Hilo, M.; O'Grady, K.; Chantrell, R.W. Susceptibility phenomena in a fine particle system: II. Field dependence of the peak. *J. Magn. Magn. Mater.* **1992**, *114*, 307–313. [CrossRef]
13. Farle, M. Ferromagnetic resonance of ultrathin metallic layers. *Rep. Prog. Phys.* **1998**, *61*, 755–826. [CrossRef]
14. Berger, R.; Bissey, J.-C.; Kliava, J.; Daubric, H.; Estournès, C. Temperature dependence of superparamagnetic resonance of iron oxide nanoparticles. *J. Magn. Magn. Mater.* **2001**, *234*, 535–544. [CrossRef]
15. Raikher, Y.L.; Stepanov, V.I. The effect of thermal fluctuations on the FMR line shape in dispersed ferromagnets. *Sov. Phys. JETP.* **1992**, *75*, 764–771.
16. Mørup, S. Comment on "Deviation from the Bloch $T^{3/2}$ Law in Ferrite Nanoparticles" by K. Mandal et al. *Europhys. Lett.* **2007**, *77*, 27003. [CrossRef]
17. Sappey, R.; Vincent, E.; Hadacek, N.; Chaput, F.; Boilot, J. Nonmonotonic Field Dependence of the Zero-Field Cooled Magnetization Peak in Some Systems of Magnetic Nanoparticles. *Phys. Rev. B—Condens. Matter Mater. Phys.* **1997**, *56*, 14551. [CrossRef]
18. Kalanda, N.; Garamus, V.; Avdeev, M.; Zheludkevich, M.; Yarmolich, M.; Serdechnova, M.; Florian Wieland, D.C.; Petrov, A.; Zhaludkevich, A.; Sobolev, N. Small-Angle Neutron Scattering and Magnetically Heterogeneous State in $Sr_2FeMoO_{6-\delta}$. *Phys. Status Solidi B* **2019**, *256*, 1800428. [CrossRef]
19. Néel, L. Théorie Du Traînage Magnétique Des Ferromagnétiques En Grains Fins Avec Application Aux Terres Cuites. *Ann. Geophys.* **1949**, *5*, 99–136.
20. Brown, W.F. Thermal Fluctuations of a Single-Domain Particle. *Phys. Rev.* **1963**, *130*, 1677–1686. [CrossRef]
21. Cullity, B.D.; Graham, C.D. *Introduction to Magnetic Materials*; John Wiley & Sons, Inc.: Hoboken, NJ, USA, 2008; p. 384.
22. Zener, C. Classical Theory of the Temperature Dependence of Magnetic Anisotropy Energy. *Phys. Rev.* **1954**, *96*, 1335–1337. [CrossRef]
23. Chien, C.L. Granular Magnetic Solids (Invited). *J. Appl. Phys.* **1991**, *69*, 5267–5272. [CrossRef]
24. Bean, C.P.; Livingston, J.D. Superparamagnetism. *J. Appl. Phys.* **1959**, *30*, S120–S129. [CrossRef]
25. Nosach, T.; Mullady, G.; Leifer, N.; Adyam, V.; Li, Q.; Greenbaum, S.; Ren, Y. Angular dependence of spin-wave resonance and relaxation in half-metallic Sr_2FeMoO_6 films. *J. Appl. Phys.* **2008**, *103*, 07E311. [CrossRef]
26. Suchaneck, G.; Artiukh, E. Magnetoresistance of antiphase boundaries in $Sr_2FeMoO_{6-\delta}$. *Phys. Status Solidi* **2021**. [CrossRef]
27. Osborn, J.A. Demagnetizing Factors of the General Ellipsoid. *Phys. Rev.* **1945**, *67*, 351. [CrossRef]

28. Bødker, F.; Mørup, S.; Linderoth, S. Surface Effects in Metallic Iron Nanoparticles. *Phys. Rev. Lett.* **1994**, *72*, 282. [CrossRef]
29. Mamiya, H.; Fukumoto, H.; Cuya Huaman, J.L.; Suzuki, K.; Miyamura, H.; Balachandran, J. Estimation of Magnetic Anisotropy of Individual Magnetite Nanoparticles for Magnetic Hyperthermia. *ACS Nano* **2020**, *14*, 8421–8432. [CrossRef]
30. Vassiliou, J.K.; Mehrotra, V.; Russell, M.W.; Giannelis, E.P.; McMichael, R.D.; Shull, R.D.; Ziolo, R.F. Magnetic and Optical Properties of γ-Fe_2O_3 Nanocrystals. *J. Appl. Phys.* **1993**, *73*, 5109. [CrossRef]
31. Evans, R.F.L.; Fan, W.J.; Chureemart, P.; Ostler, T.A.; Ellis, M.O.A.; Chantrell, R.W. Atomistic spin model simulations of magnetic nanomaterials. *J. Phys. Condens. Matter* **2014**, *26*, 103202. [CrossRef]
32. Guimarães, A.P. *Principles of Nanomagnetism*, 2nd ed.; Springer: Berlin, Germany, 2009; pp. 56–58.
33. Heider, F.; Williams, W. Note on Temperature Dependence of Exchange Constant in Magnetite. *Geophys. Res. Lett.* **1988**, *15*, 184–187. [CrossRef]